Gerd Mikolajczyk, Li Huang, Michaela Wilhelm, Wolfgang Dreher, Stefan Odenbach

Colloid deposition in monolithic porous media – Experimental investigations using X-ray computed microtomography and magnetic resonance velocimetry

Recommended Citation (primary publication/Version of Record) incl. DOI:

Gerd Mikolajczyk, Li Huang, Michaela Wilhelm, Wolfgang Dreher, Stefan Odenbach,
Colloid deposition in monolithic porous media – Experimental investigations using X-ray computed microtomography and magnetic resonance velocimetry,
Chemical Engineering Science, Volume 175, 2018, Pages 257-266, ISSN 0009-2509,
https://doi.org/10.1016/j.ces.2017.09.054

Colloid deposition in monolithic porous media – Experimental investigations using X-ray computed microtomography and magnetic resonance velocimetry

Gerd Mikolajczyk [a,*], Li Huang [b], Michaela Wilhelm [c], Wolfgang Dreher [b], Stefan Odenbach [a]

[a] Chair of Magnetofluiddynamics, Measuring and Automation Technology, Institute of Fluid Mechanics, Technical University of Dresden, 01062 Dresden, Germany
[b] In-vivo-MR Group, Faculty 02 (Biology/Chemistry), University of Bremen, 28359 Bremen, Germany
[c] Advanced Ceramics Group, Faculty 04 (Production Engineering – Mechanical Engineering and Process Engineering), University of Bremen, 28359 Bremen, Germany

HIGHLIGHTS

- Two imaging modalities were used to investigate colloid deposition.
- Particle deposition sites were captured in discrete time steps by μCT.
- The fluid flow within the filter was quantitatively measured by MRV.
- Particle deposition in individual pores is dependent on flow.
- A new type of model filter – a monolithic porous ceramic – was used.

GRAPHICAL ABSTRACT

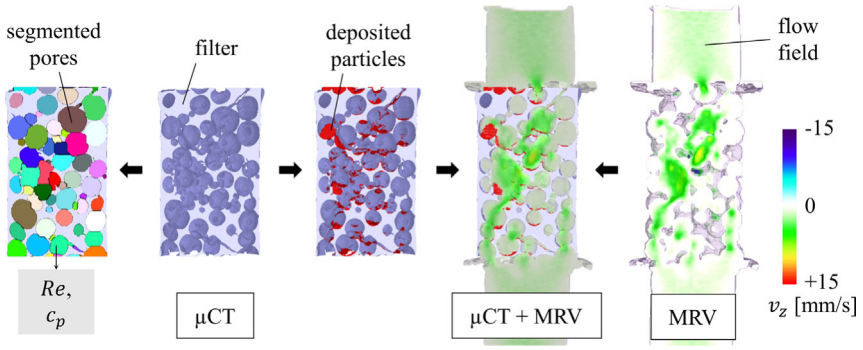

ARTICLE INFO

Article history:
Received 1 June 2017
Received in revised form 16 August 2017
Accepted 29 September 2017
Available online 30 September 2017

Keywords:
Deep bed filtration
X-ray computed microtomography
Magnetic resonance
Image registration

ABSTRACT

For experimental investigations of colloid retention in porous media, also denoted as deep bed filtration, X-ray computed microtomography (μCT) has become a basic tool within the last decade. On the one hand, μCT can spatially resolve particle deposition at discrete points of filtration time. On the other hand, the topological information of the porous media including the porosity and the pore size distribution can be obtained. Aside from structural parameters, the velocity field of the fluid within the pores, which cannot be measured by means of μCT, plays an important role in the underlying mechanisms of particle transport and immobilization. In a given structure, a high flow rate will result in increased velocity gradients as well as increased shear forces compared to a lower flow rate. High shear forces are in turn unfavorable for particle deposition. Another imaging modality, magnetic resonance velocimetry (MRV), is capable of quantifying the desired velocity maps. We demonstrate an experimental approach that combines both, MRV and μCT. In contrast to the majority of other investigations about colloid retention, the porous media investigated in this work are monolithic foam-like structures. The evaluation of colloid deposition in those monolithic filters is based on analyzing individual pores. Particle deposition in a pore is expressed by the volumetric fraction of particles while the pore flow is described by the Reynolds number. Results indicate that pores with high Reynolds numbers are not among the pores with the highest or lowest volume fraction of particles for a given time. The particle volume fraction in pores with low Reynolds numbers is mainly a function of the axial position of the pore.

* Corresponding author.
E-mail address: gerd.mikolajczyk1@tu-dresden.de (G. Mikolajczyk).

https://doi.org/10.1016/j.ces.2017.09.054
0009-2509/

1. Introduction

The transport and deposition of colloidal particles in porous media are present in many natural and technological processes, such as oil extraction (Moghadasi et al., 2004), waste water treatment (Yao et al., 1971; Xu et al., 2006) and subsurface contaminant transport (McDowell-Boyer et al., 1986; Kretzschmar et al., 1999). Usually, the particles are suspended in a liquid and their sizes are significantly smaller than the pore size of the filter. In this case, the particles are able to penetrate the porous medium and deposit at the inner surface. This process is also denoted as deep bed filtration.

The mechanisms of particle retention are subdivided into two groups (Ives, 1975; McDowell-Boyer et al., 1986). Sedimentation, gravity, interception, inertia and hydrodynamic forces lead the particles towards the inner surface of the porous medium. The immobilization of particles at the inner surface is due to electrostatic and van-der-Waals-forces (Derjaguin and Landau, 1941; Verwey and Overbeek, 1948) as well as wedging or straining (Johnson et al., 2010). However, due to the complexity of the process it is an up-to-date challenge to predict the particle deposition in a given filter.

The main challenges in experimental investigations of deep bed filtration processes are the high opacity of the porous media and the small particle sizes in the range of typically a few nanometers to some microns. Being able to cope with those issues, X-ray computed microtomography (μCT) has become a basic tool in the investigation of particle retention in the last decade (e.g. Al-Abduwani et al., 2005; Li et al., 2006; Gaillard et al., 2007; Long et al., 2010; Günther and Odenbach, 2016). Different linear absorption coefficients of the particles, the carrier liquids and the porous media respectively result in three-dimensional gray value images of the materials. By performing digital image processing on the images the spatial distribution of the deposited particles and the topological information of the filters can be obtained. In addition to the topological parameters of the filters, particle retention is also fundamentally controlled by the fluid flow (Mays and Hunt, 2005; Bradford et al., 2009; Li et al., 2010). In a given structure, an increased velocity results in higher shear forces and thus a decreased filtration efficiency (Yao et al., 1971). Bedrikovetsky et al. (2012) showed that the maximum retained volume fraction of particles is a function of the fluid velocity. The decisive information of the fluid velocity within the pores, however, cannot be obtained by means of μCT. To this end, magnetic resonance velocimetry (MRV) was applied in this work to measure the velocity maps of the carrier liquid. For reviews see e.g. Elkins and Alley (2007) or Gladden and Sederman (2013). This velocimetry method is used for instance in medicine to quantitatively visualize the blood flow in vessels. The correlation of particle deposition and fluid velocity has been investigated in filtration processes different from deep bed filtration by means of magnetic resonance (MR, Dirckx et al., 2000; Buetehorn et al., 2011). Also Bray et al. (2017) recently used μCT and MRV to study mineral precipitation in porous media.

Most of the researches in deep bed filtration were done by using model systems of porous media such as packed beds of glass beads (e.g. Li et al., 2006; Yoon et al., 2006; Chen et al., 2009; Waske et al., 2012). Packed beds of sand grains, which are closer to natural processes and industrial applications, have also been investigated (Johnson et al., 1996; Al-Abduwani et al., 2005; Li et al., 2006; Xu et al., 2006). Consequently, the porous media were generally packed beds. Colloid retention in monolithic filters like ceramic, metallic or polymer foams (Purchas and Sutherland, 2002) has rarely been investigated (Brosten et al., 2010). To overcome this shortcoming, we introduced a new type of model filter that represents the cavity of a packed bed of spheres. Those monolithic ceramic filters are open-pored and resemble ceramic foam-like filters.

2. Materials and methods

2.1. General procedure

The transport and deposition of colloids within a porous medium were experimentally investigated by combining μCT and MRV. Firstly, MRV was used to measure the fluid velocity (without particles) within the porous medium. Subsequently, a suspension was pumped through the porous medium and a series of μCT scans was performed in order to image the temporal evolution and spatial distribution of deposited particles. Eventually, both 3D image data sets were combined using image registration.

The velocity field within the porous medium might have changed after particle deposition due to deposited particles that add to the solid (filter) phase. However, additional MRV measurements were not carried out because deposited particles might move when the samples are moved between the μCT- and MR-scanner. Accordingly, only the velocity fields within the porous media prior to particle deposition were obtained.

2.2. Materials and experimental setup

Monolithic and open-pored polymer derived ceramics (*cf.* Fig. 1a) were used as porous filter media. In total three samples with similar properties (*cf.* Table 1) with regard to pore size, porosity, sample size and surface characteristics were consecutively investigated. The samples were of a cylindrical shape with a diameter D of approximately 9.5 mm and a height H of approximately 16 mm. The ceramic surfaces showed hydrophilic characteristics in water and n-heptane adsorption experiments. The porosity and pore sizes were calculated from μCT images. Across all porous media, the volume-averaged porosity was 70% ± 2% whereas the median diameter of the spherically shaped pores was 1.9 mm ± 0.1 mm. The spherical pore shape is due to the production routine described in (Adam et al., 2014). A polypropylene mold was filled with expanded polystyrene beads (2 mm in size, Klassen Vitali, Germany) and subsequently infiltrated with a polymer solution consisting of 86 wt% of methyl phenyl polysiloxane (H44, Wacker Chemie AG, Germany) and 14 wt% of 3-aminopropyltriethoxysilane (APTES, abcr GmbH, Germany). Afterwards, the volume of the mold was compressed by 6.25% while the excessive polymer was drained. Furthermore, the samples were cross-linked at room-temperature and 100 °C and the pyrolytic conversion was performed at 1000 °C under nitrogen. The pore space resulted from the decomposition and evaporation of the polystyrene beads. Accordingly, the ceramic phase represents the cavity of a packed bed of beads.

Tin (IV) oxide particles (SnO_2, Kremer Pigmente GmbH & Co. KG, Germany) were selected as the colloidal phase. The density is reported by the manufacturer to be 6.95 g/cm^3 whereas the median particle diameter was determined by laser diffraction (HELOS/KR-H2487, Sympatec GmbH, Germany) to be 0.85 μm. The particles were diluted in distilled water with a volume fraction of 0.01 vol% throughout all experiments.

A dedicated flow cell (*cf.* Fig. 1b) was designed under the framework conditions to be used in μCT- and MR-scanners alike, preventing flow bypasses and ensuring a fully developed flow profile at the inlet of the porous medium. The porous media were mounted between two adapters with an inner diameter of 8mm and sealed by heat-shrink tubing. To avoid additional MR signals, the adapters were made of polytetrafluoroethylene (PTFE), which is free of hydrogen nuclei and non-magnetic. In order to prevent flow bypasses the flexible heat-shrink tubing was necessary due to slightly varying diameters of the monolithic porous media.

For the column experiments (*cf.* Fig. 1c) the suspension was pumped through the flow cell via a peristaltic pump (REGLO

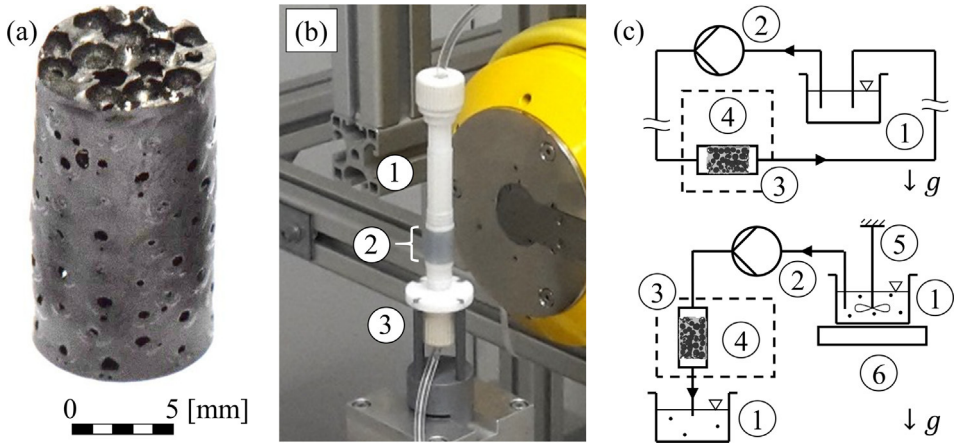

Fig. 1. (a) A photo of an investigated porous filter. (b) The mounted flow cell in the in-house developed μCT scanner (background: X-ray source). 1 – inlet, 2 – filter position, 3 – outlet. (c) Scheme of the experimental setups. Top: MRV, bottom: μCT. 1 – reservoir, 2 – peristaltic pump, 3 – flow cell including filter, 4 – MR scanner (top)/μCT scanner (bottom), 5 – stirrer, 6 – magnetic stirrer, gravitational acceleration g.

Table 1
Characteristics of the porous media.

Sample number	Porosity (%)	Median pore diameter (mm)	Dimension (mm) diameter D × height H
1	71.5	1.81	9.2 × 16.4
2	68.6	1.88	9.6 × 16.1
3	71.9	1.99	9.9 × 15.1

Analog MS-2/6, Cole-Parmer GmbH, Germany) with a volumetric flow rate of about 50 mm^3/s, which is approximately one tenth of the pore volume of the porous medium per second. This corresponds to a mean approach velocity in the adapter of the flow cell of $\bar{v}_\infty = 1$ mm/s. The suspension in the reservoir was constantly stirred, both mechanically and by using a magnetic stirrer. Prior to the filtration experiments, the reservoir (containing the suspension) was ultrasonically treated (Sonorex TK52, Bandelin electronic GmbH & Co. KG, Germany) for 5 min to break up particle agglomerates. The effluent was collected separately. During the MRV measurements the pulsation effect of the peristaltic pump is regarded as negligible due to the length of the tube (>3 m) between the pump and the filtration cell.

Prior to the MRV measurements as well as the filtration experiments, the flow cell including the porous medium had to be prepared in order to fully saturate the pores with water. To this end, the flow cell and connecting tubes were rinsed with distilled water to achieve pore pre-saturation. Subsequently, the components were placed in a flooded desiccator, which was sealed and evacuated from top by a vacuum pump. Remaining air bubbles degassed due to the low pressure. As a result, the content of air within the flow cell was reduced to less than 0.1 vol% which could directly be observed from the MR/μCT scans of the flow cell.

2.3. Magnetic resonance velocimetry (MRV)

A horizontal 7T MR imaging system (Bruker BioSpec 70/20 USR, Bruker BioSpin MRI GmbH, Germany) was used to image the fluid velocity within the pores. The MR scanner is equipped with a 114 mm bore gradient system (B-GA 12S2, Bruker BioSpin MRI GmbH, Germany) and controlled by ParaVision 5.1 (Bruker BioSpin MRI GmbH, Germany) on a Linux workstation. Due to limited vertical space within the MR scanner, the flow cell was mounted horizontally (perpendicular to gravitational force). During MRV measurements, distilled water (without particles) was used as flowing liquid.

The MRV was based on a phase contrast MR method. This method was customized for slow liquid flow in porous media in order to enable the quantification of the fluid velocity within the pores. Spin echo based velocity encoding was performed within the observation time $\Delta = 8$ ms. With a maximum observed velocity of 30 mm/s and under the assumption of stationary flow only intra-pore movements of spins took place. A detailed description of the customized method can be found in Huang et al. (2017). As a result, a data set of three images that contain the x-, y- and z- component of the velocity field within a filter were obtained. Features of the measurements such as the velocity encoding range (VENC) that is defined as [-VENC, VENC] and the signal-to-noise ratio (SNR) of the MR images along with other experimental details are summarized in Table 2.

2.4. X-ray computed microtomography (μCT)

A laboratory μCT scanner (*cf.* Shevchenko et al., 2013) was used to image the porous media and the temporal evolution of the particle deposition. As the X-ray source, a nano-focus tube (XS160NFOF, GE Measurement and Control Solutions, USA) with a tungsten target was used. The acceleration voltage was set to 90 kV and the cathode current was set to 170 μA. The attenuated X-rays were captured by using a detector (Shad-o-Box 4K EV, Rad-icon Imaging Corporation, USA) with a resolution of 2048 × 2000 pixel (horizontal × vertical), a corresponding pixel spacing of 48 μm and a digitization of 12 bit. Radiographs were taken with an angular increment of 0.25° over a full rotation of 360°. The magnification due to the cone beam was 4.2. Reconstruction was based on a FDK-algorithm (Feldkamp et al., 1984) and the resulting voxel edge length of the reconstructed tomogram was 23 μm due to a binning of 2.

A series of μCT scans was performed in discrete steps of filtration time. Starting with a filtration time t of 7.5 min a new scan was performed whenever filtration time doubled. Consequently, additional scans were done after 15 min, 30 min, 60 min, 120 min, 240 min and eventually, as an exception of the rule, after 360 min of filtration. Furthermore, a μCT scan prior to filtration was done. A single μCT scan required an acquisition time of approximately 60 min. During data acquisition, the pump was switched off in order to avoid motion artifacts of moving particles. In contrast to the MRV measurements, the flow cell was mounted vertically (in direction of gravity) during filtration experiments so that the mean flow velocity and the sedimentation velocity pointed in the same direction.

Table 2
Experimental details of the MRV measurements.

Sample number	VENC [x,y,z] (mm/s)	SNR of MR images (–)	Scanning time of single scan (h)	Spatial resolution (μm)
1	[30,30,30]	94.7	3.3	200 × 200 × 200
2	[15,15,30]	197	8.0	
3	[10,10,20]	179	8.0	

Sample number	Echo time (TE) of the first echo (ms)	Repetition time (TR) (ms)	Velocity encoding gradient ...		
			Duration (ms)	Separation (ms)	Strength [x,y,z] (mT/m)
1	8	600	0.37	8	[32.9,32.9,32.9]
2		1000			[65.8,65.8,32.9]
3		1000			[98.6,98.6,49.4]

However, the profile of a tubular laminar flow is not dependent on the orientation of the tube (Sigloch, 2009).

2.5. Data processing

In the resulting 3D MR and μCT images the voxel size and orientation of the flow cell within the images were intrinsically different. To address this, MR images were manually registered to the μCT scans utilizing fiducial markers (*cf.* Figs. 2 and 3, white arrows) and using the freeware 3DSlicer, version 4.5 (http://www.slicer.org, Fedorov et al., 2012).

The evaluation of μCT images required an additional post processing step. Due to fluctuations of the X-ray source, areas that contain the same material can have varying mean gray values in subsequent reconstructed μCT scans. To enable a comparison among a series of μCT images a calibration was required. To this end, the mean gray value of two materials, which needed to be present in every μCT image, was taken as the basis for a linear gray value adjustment of all voxels.

The μCT images were further processed by applying a median filter (elliptical shape, radius of 3.5 voxel) in order to reduce image noise. By doing so a binarization of the μCT images was possible using a consistent threshold for all samples. Matlab R2014a (The MathWorks Inc., USA) and the Matlab plug-in DIPimage, version 2.8 (Quantitative Imaging Group, Delft University of Technology), were generally used for image processing, except if noted otherwise.

The 3D μCT and MR images were further processed in order to evaluate the time-dependent volumetric fraction of particles c_p, the Reynolds number Re and an approximated mean shear stress $\bar{\tau}_{vm}$ of individual pores of the porous media. To this end the μCT scans of the filter at $t = 0$ were binarized based on the histogram and the pore space, consisting of connected pores, was segmented in individual pores using a watershed algorithm (Beucher and Lantuéjoul, 1979). The diameter of each pore was then computed from the pore volume V_{pore} as equivalent diameter of a sphere

$$d_{pore} = \sqrt[3]{\frac{6}{\pi} \cdot V_{pore}}. \quad (1)$$

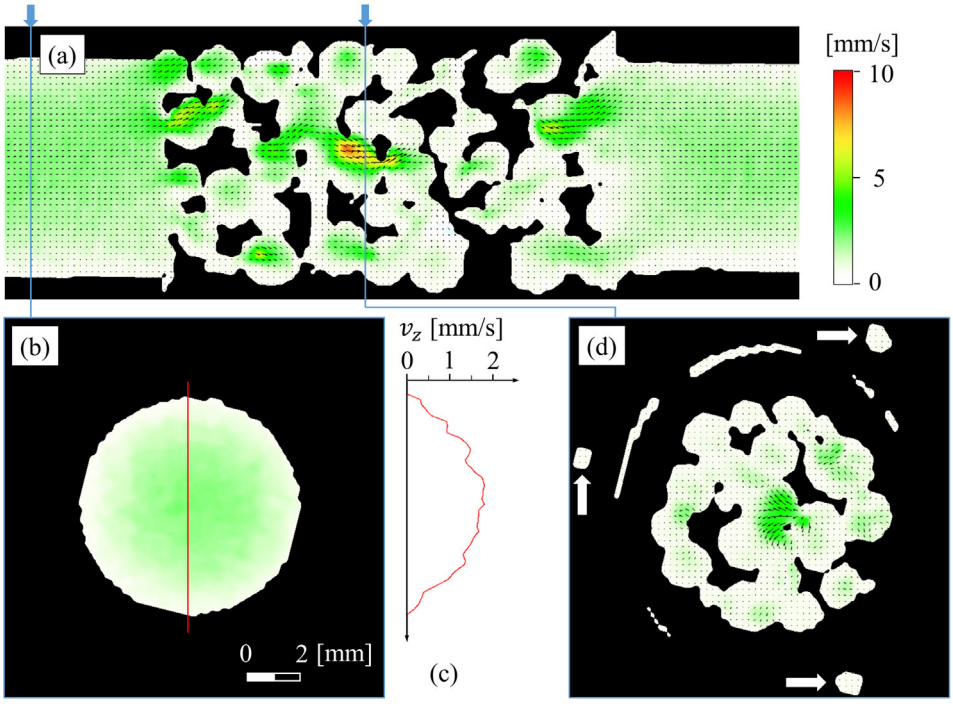

Fig. 2. Representative cross-sectional MR images after registration. (a) The z-component of the velocity in a central axial cross-section is visualized by the color map (top right). The vector field represents the y- and z-component of the velocity. (b) The z-component of the velocity in a radial cross-section within the inlet is visualized by the color map. (c) 1D plot of the z-component of the velocity along the line in subfigure (b). (d) The combined x- and y-velocity components in the radial cross-section within the porous medium are visualized by the color map and the vector field. The white arrows indicate the steady water content of the three fiducial markers. The ring-shaped area between the fiducials and the pores are due to static water trapped in the sealing of the flow cell (*cf.* Fig. 3). The axial positions of the radial cross-sectional images (b) and (d) are indicated by the blue arrows.

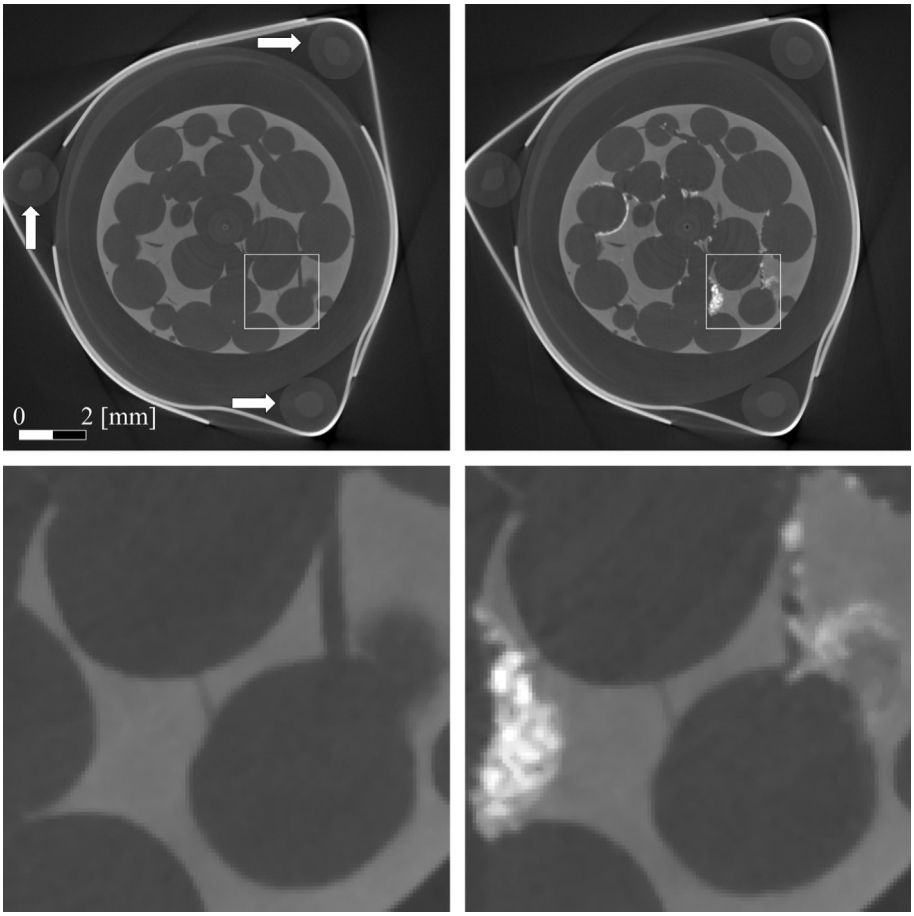

Fig. 3. Representative post processed cross-sectional gray value images of μCT scans. Left column: Prior to filtration. Right column: After 30 min of filtration. Top row: Flow cell including fiducial markers (indicated by arrows). Bottom row: Enlarged view of the pore structure (white rectangle). The porous ceramic medium (light gray) is filled with water (dark gray) and deposited particles (white, right column). Also visible are cracks in the ceramic phase that originate from the manufacturing.

Furthermore, the volume of particles $V_p(t)$ per pore and filtration time t was determined by using a consistent threshold in order to binarize the μCT images at filtration times $t > 0$. The particle phase has the highest mean gray value among the imaged materials. The threshold was chosen so that all other materials are just not binarized. A volume fraction of particles per pore was then calculated by normalizing the particle volume within a pore with the corresponding pore volume

$$c_p = \frac{V_p(t)}{V_{pore}}. \tag{2}$$

Additionally, the velocity magnitude of the velocity maps was calculated as $v_m = \sqrt{v_x^2 + v_y^2 + v_z^2}$ as a voxel based operation and the arithmetic mean velocity magnitude per pore $\bar{v}_m$ was computed. Subsequently, the Reynolds number Re of each pore was determined

$$Re = \frac{\bar{v}_m \cdot d_{pore}}{\nu} \tag{3}$$

with the kinematic viscosity $\nu = 1 \cdot 10^{-6}$ m^2/s of water at room temperature (20 °C). Eventually, the mean shear stress $\bar{\tau}_{vm}$ per pore was estimated based on the velocity magnitude. To this end, the gradient of the velocity magnitude was computed

$$\nabla v_m = \frac{1}{2l} \cdot \begin{pmatrix} v_m(x+1,y,z) - v_m(x-1,y,z) \\ v_m(x,y+1,z) - v_m(x,y-1,z) \\ v_m(x,y,z+1) - v_m(x,y,z-1) \end{pmatrix} \tag{4}$$

at the position of a voxel (x, y, z) with the edge length of a voxel l. Subsequently, the shear stress was determined as a voxel based operation

$$\tau_{vm} = \eta \cdot |\nabla v_m| \tag{5}$$

with the dynamic viscosity $\eta = 1 \cdot 10^{-3}$ Pa s of water at room temperature (20 °C). For a laminar tube flow the exact analytical shear stress distribution is obtained by the proposed approach. Based on the shear stress maps the arithmetic mean shear stress per pore $\bar{\tau}_{vm}$ was calculated.

3. Results

3.1. MR images

Representative registered cross-sectional MR images can be seen in Fig. 2. By definition, the direction of the z-axis corresponds to the main flow direction. The z-component of the velocity is displayed in Fig. 2a in an axial cross-section and in Fig. 2b in a radial cross-section by the color-map respectively. The parabolic profile of a fully developed flow in the inlet of the flow cell can be observed in Fig. 2b and c. Fig. 2d displays the x- and y-components of the velocity in a radial cross-section within the porous medium. The circumferentially attached fiducial markers are indicated by white arrows. A three-dimensional visualization of the fluid velocity within the pores can be realized by computing the streamlines on the basis of the vector components of the

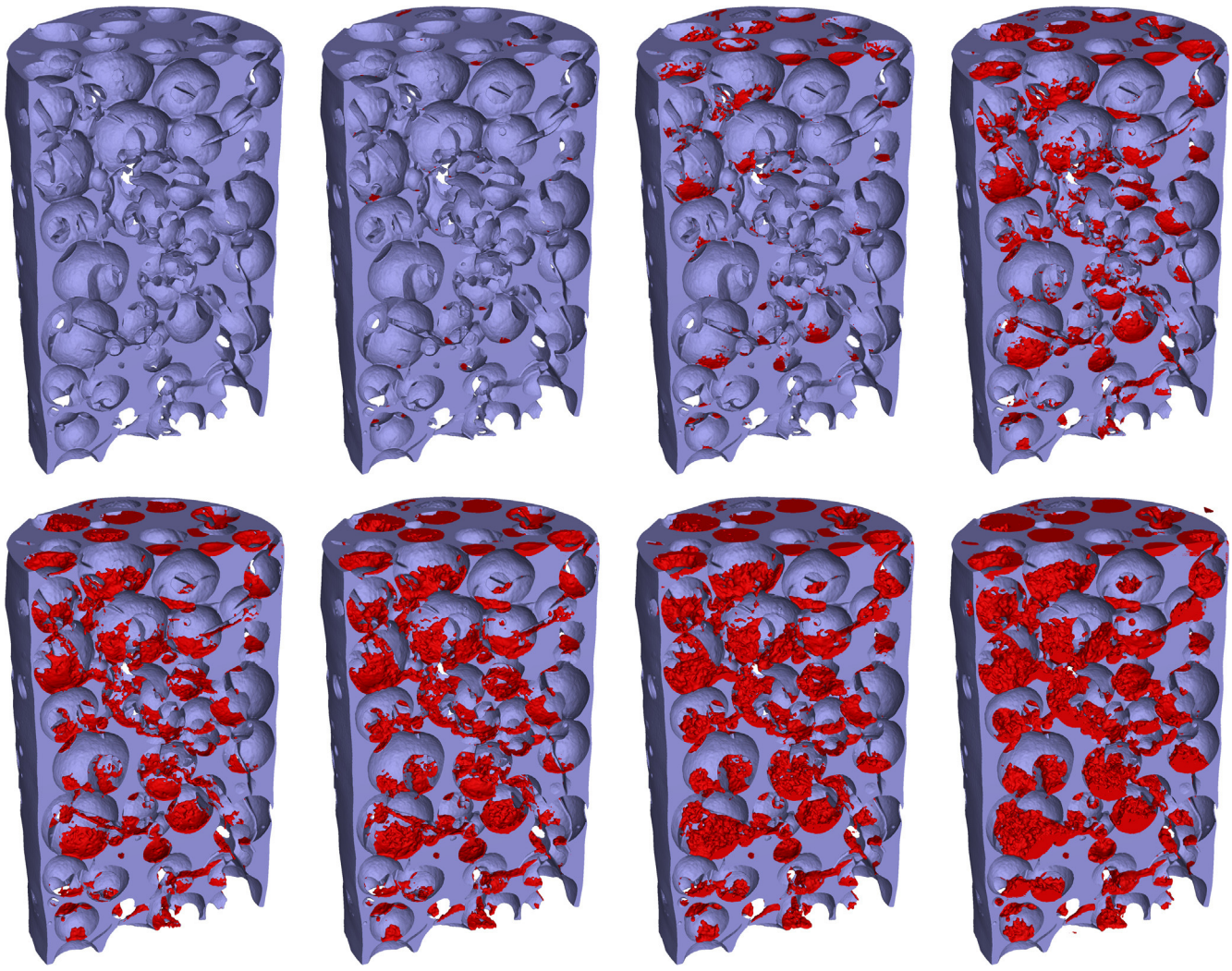

Fig. 4. Cross-sectional rendered CT images of sample 2 for all investigated times of filtration t (top row from left to right: before filtration, 7.5 min, 15 min, 30 min; bottom row from left to right: 60 min, 120 min, 240 min, 360 min). Particle deposition sites within the filter (violet) are displayed in red.

velocity. To this end, ParaView, version 5.2 (Kitware Inc., LANL & SNL, USA), was used. An example is shown in the supplementary material to this article (Fig. A.1).

3.2. μCT images

Representative post processed cross-sectional images of μCT scans are displayed in Fig. 3. For comparison the top row of Fig. 3 displays a cross-sectional view (the same as in Fig. 2d) of the flow cell at two different times of filtration. On the left the porous medium is shown prior to filtration, whereas on the right first deposition sites of particles after 30 min of filtration are visible. The median particle size of 0.85 μm is significantly smaller than the spatial resolution of the μCT scans (voxel size of 23^3 μm^3). However, due to the high atomic number of tin and the high density of tin (IV) oxide (6.95 g/cm^3) the particles exhibit a high absorption coefficient of X-rays, which results in an increased gray value of the according voxels and thus in a sufficient contrast compared to the porous medium and water.

Accordingly, single particles cannot be resolved and the volume fraction of particles per pore c_p is only approximated. The three fiducial markers are indicated by arrows as in Fig. 2d. In Fig. 4 the temporal evolution of particle deposition sites in sample 2 is qualitatively displayed by cross-sectional rendered μCT images for all investigated times of filtration t. The rendering was done by using the software VGStudio MAX, version 2.1 (Volume Graphics, Germany).

3.3. Data evaluation

In Fig. 5 the logarithmically scaled volume fraction of particles c_p is plotted against the Reynolds number Re for all pores of the investigated porous media. Each data point within a single diagram represents a single pore within that sample. All three investigated porous media at four representative times of filtration are displayed. With increasing time of filtration, the volume fraction of particles per pore increased successively. At early times of filtration particle deposition was limited to a small amount of pores. Thus, after 7.5 min of filtration less pores are displayed compared to later times of filtration. After approximately 4...6 h of filtration, the volume fraction of particles was as high as 100% in some individual pores near the inlet throughout all samples. Note that the Reynolds number based on the median pore diameter $\bar{d}_{pore} = 1.9$ mm and the mean velocity within the sample $\bar{v} = \bar{v}_\infty/\varepsilon \approx 1.4$ mm/s (mean approach velocity $\bar{v}_\infty = 1.0$ mm/s, porosity $\varepsilon \approx 0.7$) equals approximately $\overline{Re} \approx 2.5 \ldots 2.8$. The distribution of Reynolds

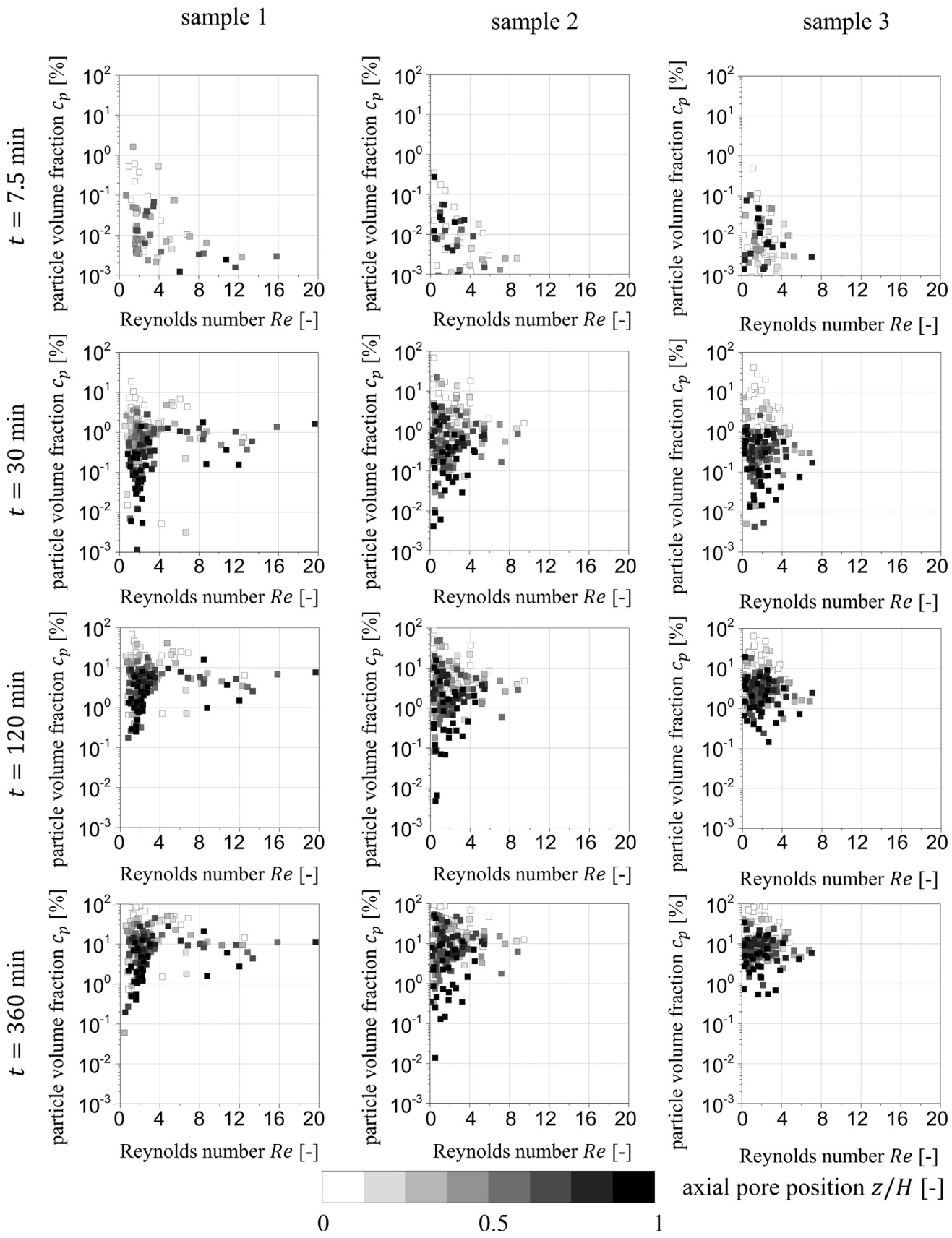

Fig. 5. Plots of the volume fraction of particles c_p versus the Reynolds number *Re* of the individual pores at 4 different times of filtration *t*. The position of the pore normalized by the sample height *H* in the direction of the mean flow (z-direction) starting at the inlet of the porous medium is indicated by the gray value gradation.

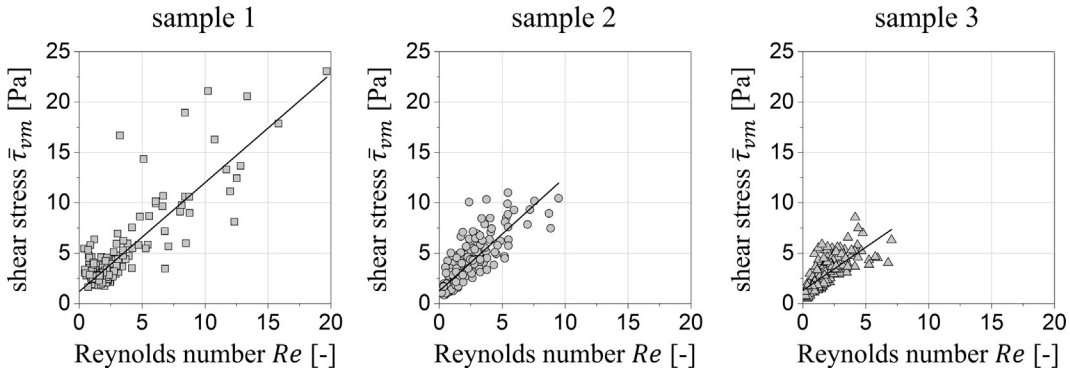

Fig. 6. Plots of the pore-averaged shear stress based on the velocity magnitude versus the Reynolds number per pore. The positive correlation between both physical quantities is emphasized by a best fit straight line.

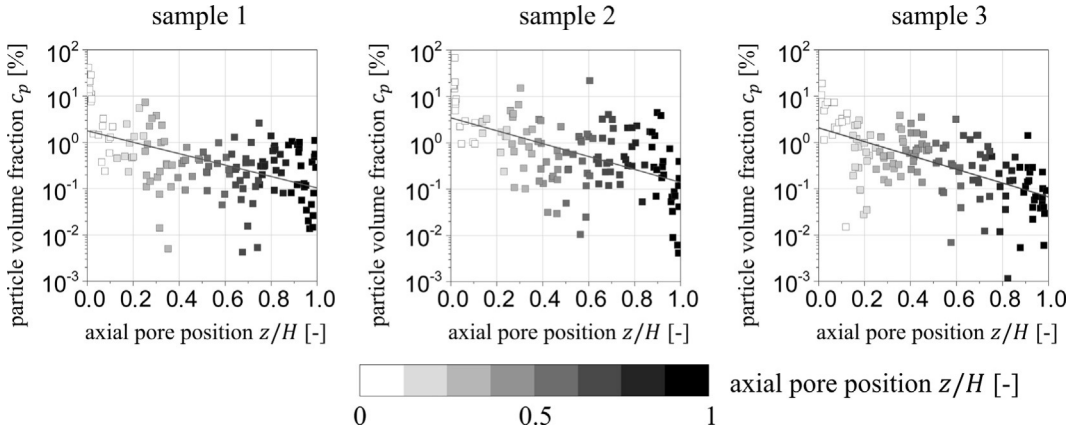

Fig. 7. Plots of the volume fraction of particles c_p after a filtration time of $t = 30$ min versus the axial pore position normalized by the sample height H (also indicated by the gray value gradation in correspondence to Fig. 5). Only pores with a Reynolds number $Re < \overline{Re}$ were considered. The exponential decrease of the particle volume fraction is emphasized by a best fit straight line based on the logarithmical data.

numbers within the samples is plotted in Fig. A.2 in the supplementary material to this article.

Based on Eq. (5) the mean shear stress per pore was estimated and compared to the related Reynolds number. The result for every pore among the investigated samples is plotted in Fig. 6. The plots indicate that there is a positive correlation between the Reynolds number and the mean shear stress within a pore for the investigated flow regime.

4. Discussion

The characteristic plots in Fig. 5 indicate that the Reynolds number per pore has an influence on the deposition kinetics of particles and consequently the volume fraction of particles per pore.

As a direct observation from Fig. 5 it can be seen that pores, which feature a high Reynolds number, are not among the pores with high or low volume fractions of particles for a given time of filtration. This can be explained as follows. High Reynolds numbers correspond to high mean shear stresses for the investigated flow rate as indicated by Fig. 6. A high shear stress within a fluid is not favorable for particle retention due to high resulting forces that counteract particle deposition. Accordingly, for the investigated flow regime high volume fractions of particles are unlikely in pores with high Reynolds numbers.

On the other hand, despite a low efficiency of particle deposition in such pores, a minimal particle retention is likely due to a high influx of suspended particles. Accordingly, lowest volume fractions of particles are also unlikely in pores with a high Reynolds number.

Pores with a low Reynolds number exhibit volumetric fractions of particles which differ by several orders of magnitude. In such pores the volume fraction of particles is governed by the position of the pore in the direction of flow, which is indicated by the gray value gradation in Fig. 5 (white pores are close to the inlet whereas black pores are further downstream). For comparison, the volumetric fraction of particles c_p after a filtration time of $t = 30$ min is logarithmically plotted versus the dimensionless axial pore position in Fig. 7 considering pores with a Reynolds number $Re < \overline{Re}$ only. As Fig. 7 indicates the particle volume fraction c_p decreases on average exponentially in mean flow direction. In principal, this is in agreement with the classical colloid filtration theory (CFT, *cf.* Yao et al., 1971). The CFT predicts an exponential decrease of the particle volume fraction in the suspension c_l in the flow direction. As a consequence, the volume fraction of deposited particles theoretically also decreases exponentially in axial direction.

In order to predict the volume fraction of particles in individual pores at a given time of filtration other parameters apart from the axial position of the pore are relevant as well. This can directly be observed from Fig. 7, where some pores exhibit higher volume fractions of deposited particles compared to pores that are further upstream and vice versa.

One example of such parameters could be the topological environment of an individual pore. For instance, if pores are aligned in the mean flow direction it could be assumed that particles tend to

deposit in the most downstream pore due to sedimentation. In order to quantify the complex topological characteristics an approach is required in the future.

As stated above, CFT predicts an exponential decrease of the particle volume fraction in the suspension c_l in the flow direction. While this can be expected to be true on average, individual pores that are in the same axial position could be exposed to varying volume fractions of suspended particles – for instance due to heterogeneous particle retention upstream. However, the volume fraction of suspended particles c_l within the porous medium cannot be obtained from the demonstrated experimental approach up to now.

Across the three samples the diagrams in Fig. 5 are generally in good qualitative and quantitative agreement. As a difference, sample 1 features several pores with higher Reynolds numbers in comparison to the other two samples. The reason are irregularities in the topology of that sample. The pores with the highest Reynolds numbers in sample 1 form an exceptionally pronounced non-tortuous flow channel in the mean flow direction. Thus, a considerable portion of the flow rate passed through those pores, which in turn results in high velocities and Reynolds numbers respectively. This stresses the influence of the topology on the fluid flow within the pores and the particle transport. As mentioned before, the topological environment of individual pores can be seen as a significant parameter for particle retention.

The observed fluid velocity field within the pores is comparatively heterogeneous with maximum local velocity magnitudes being significantly higher than the average fluid velocity $\bar{v}$. The ratio of the maximum observed Reynolds number per sample to the respective average Reynolds number $\overline{Re}$ is as high as 7.8 for sample 1, 3.4 for sample 2 or 2.5 for sample 3.

5. Conclusions

In this work particle retention in porous media was experimentally investigated by combining two imaging modalities: X-ray computed microtomography (μCT) and magnetic resonance velocimetry (MRV). The investigated porous media were monolithic ceramic filters which resemble ceramic sponges or foams. The topology of the porous medium as well as deposition sites of particles at different times of filtration could be obtained by μCT. The quantification of the velocity field within the porous media was obtained by MRV. The resulting images of both imaging modalities could be combined by means of image registration.

The evaluation was done by studying the relation between the volumetric fraction of particles and the Reynolds number of individual pores. The Reynolds numbers were calculated from the measured velocity maps obtained by MRV. It could be shown that the pore Reynolds numbers are heterogeneously distributed. In pores with a high Reynolds number high shear forces (leading to low particle volume fractions) and a high particle influx (leading to high particle volume fractions) cause neither the highest nor the lowest particle volume fractions compared to other pores. In pores with low Reynolds numbers possible volume fractions of particles extend over several orders of magnitude for a given time of filtration. With a decreasing Reynolds number the position of the pore in the direction of the mean flow tends to govern the value of the particle volume fraction. To predict the particle volume fraction of individual pores, however, the information about the axial pore position is not sufficient. Other parameters such as the volume fraction of the particles in the suspension and its change within the porous medium need to be considered in future investigations.

Acknowledgements

This work was supported by the German Research Foundation within the Research Training Group GRK 1860 “Micro-, meso- and macroporous nonmetallic Materials: Fundamentals and Applications” (MIMENIMA) under grant number GRK 1860/1.

Appendix A. Supplementary material

Supplementary data associated with this article can be found, in the online version, at https://doi.org/10.1016/j.ces.2017.09.054.

References

Adam, M., Kocanis, S., Fey, T., Wilhelm, M., Grathwohl, G., 2014. Hierarchically ordered foams derived from polysiloxanes with catalytically active coatings. J. Eur. Ceram. Soc. 34 (7), 1715–1725. https://doi.org/10.1016/j.jeurceramsoc.2013.12.011.

Al-Abduwani, F.A.H., Farajzadeh, R., van den Broek, W.M.G.T., Currie, P.K., Zitha, P.L. J., 2005. Filtration of micron-sized particles in granular media revealed by x-ray computed tomography. Rev. Sci. Instrum. 76 (10), 103704. https://doi.org/10.1063/1.2103467.

Bedrikovetsky, P., Zeinijahromi, A., Siqueira, F.D., Furtado, C.A., de Souza, A.L.S., 2012. Particle detachment under velocity alternation during suspension transport in porous media. Transp. Porous Media 91 (1), 173–197. https://doi.org/10.1007/s11242-011-9839-1.

Beucher, S., Lantuéjoul, C., 1979. Use of watersheds in contour detection. In: Int. Workshop on Image Processing, Real-time edge and motion detection/estimation, CCETT/INSA/IRISA, IRISA Report 132, 2.1-2.12, Rennes.

Bradford, S.A., Torkzaban, S., Leij, F., Šimůnek, J., van Genuchten, M.T., 2009. Modeling the coupled effects of pore space geometry and velocity on colloid transport and retention. Water Resour. Res. 45 (2). https://doi.org/10.1029/2008wr007096.

Bray, J.M., Lauchnor, E.G., Redden, G.D., Gerlach, R., Fujita, Y., Codd, S.L., Seymour, J. D., 2017. Impact of mineral precipitation on flow and mixing in porous media determined by microcomputed tomography and MRI. Environ. Sci. Technol. 51 (3), 1562–1569. https://doi.org/10.1021/acs.est.6b02999.

Brosten, T.R., Fridjonsson, E.O., Codd, S.L., Seymour, J.D., 2010. NMR measurement of the transport dynamics of colloidal particles in an open cell polymer foam porous media. J. Colloid Interface Sci. 349 (1), 384–391. https://doi.org/10.1016/j.jcis.2010.04.050.

Buetehorn, S., Utiu, L., Küppers, M., Blümich, B., Wintgens, T., Wessling, M., Melin, T., 2011. NMR imaging of local cumulative permeate flux and local cake growth in submerged microfiltration processes. J. Membr. Sci. 371 (1), 52–64. https://doi.org/10.1016/j.memsci.2011.01.018.

Chen, C., Lau, B.L., Gaillard, J.F., Packman, A.I., 2009. Temporal evolution of pore geometry, fluid flow, and solute transport resulting from colloid deposition. Water Resour. Res. 45 (6). https://doi.org/10.1029/2008wr007252.

Derjaguin, B.V., Landau, L., 1941. Theory of the stability of strongly charged lyophobic sols and of the adhesion of strongly charged particles in solutions of electrolytes. Acta Physicochim. URSS 14 (6), 633–662.

Dirckx, C.J., Clark, S.A., Hall, L.D., Antalek, B., Tooma, J., Hewitt, J.M., Kawaoka, K., 2000. Magnetic resonance imaging of the filtration process. AIChE J. 46 (1), 6–14. https://doi.org/10.1002/aic.690460103.

Elkins, C.J., Alley, M.T., 2007. Magnetic resonance velocimetry: applications of magnetic resonance imaging in the measurement of fluid motion. Exp. Fluids 43 (6), 823–858. https://doi.org/10.1007/s00348-007-0383-2.

Fedorov, A., Beichel, R., Kalpathy-Cramer, J., Finet, J., Fillion-Robin, J.C., Pujol, S., et al., 2012. 3D Slicer as an image computing platform for the Quantitative Imaging Network. Magn. Reson. Imaging 30 (9), 1323–1341. https://doi.org/10.1016/j.mri.2012.05.001.

Feldkamp, L.A., Davis, L.C., Kress, J.W., 1984. Practical cone-beam algorithm. JOSA A 1 (6), 612–619. https://doi.org/10.1364/josaa.1.000612.

Gaillard, J.F., Chen, C., Stonedahl, S.H., Lau, B.L., Keane, D.T., Packman, A.I., 2007. Imaging of colloidal deposits in granular porous media by X-ray difference micro-tomography. Geophys. Res. Lett. 34 (18). https://doi.org/10.1029/2007gl030514.

Gladden, L.F., Sederman, A.J., 2013. Recent advances in flow MRI. J. Magn. Reson. 229, 2–11. https://doi.org/10.1016/j.jmr.2012.11.022.

Günther, S., Odenbach, S., 2016. A method for image decomposition and particle quantification in multiphase systems. Transp. Porous Media 112 (1), 105–116. https://doi.org/10.1007/s11242-016-0634-x.

Huang, L., Mikolajczyk, G., Küstermann, E., Wilhelm, M., Odenbach, S., Dreher, W., 2017. Adapted MR velocimetry of slow liquid flow in porous media. J. Magn. Reson. 276, 103–112. https://doi.org/10.1016/j.jmr.2017.01.017.

Ives, K.J. (Ed.), 1975. The scientific basis of filtration: proceedings of the NATO Advanced Study Institute held at Cambridge, UK, July 2–20, 1973, vol. 2. Noordhoff International Publishing.

Johnson, P.R., Sun, N., Elimelech, M., 1996. Colloid transport in geochemically heterogeneous porous media: Modeling and measurements. Environ. Sci. Technol. 30 (11), 3284–3293. https://doi.org/10.1021/es960053.

Johnson, W.P., Pazmino, E., Ma, H., 2010. Direct observations of colloid retention in granular media in the presence of energy barriers, and implications for inferred mechanisms from indirect observations. Water Res. 44 (4), 1158–1169. https://doi.org/10.1016/j.watres.2009.12.014.

Kretzschmar, R., Borkovec, M., Grolimund, D., Elimelech, M., 1999. Mobile subsurface colloids and their role in contaminant transport. Adv. Agron. 66, 121–193. https://doi.org/10.1016/s0065-2113(08)60427-7.

Li, X., Lin, C.L., Miller, J.D., Johnson, W.P., 2006. Pore-scale observation of microsphere deposition at grain-to-grain contacts over assemblage-scale porous media domains using X-ray microtomography. Environ. Sci. Technol. 40 (12), 3762–3768. https://doi.org/10.1021/es0525004.

Li, X., Li, Z., Zhang, D., 2010. Role of low flow and backward flow zones on colloid transport in pore structures derived from real porous media. Environ. Sci. Technol. 44 (13), 4936–4942. https://doi.org/10.1021/es903647g.

Long, W., Huang, H., Serlemitsos, J., Liu, E., Reed, A.H., Hilpert, M., 2010. Pore-scale study of the collector efficiency of nanoparticles in packings of nonspherical collectors. Colloids Surf., A 358 (1), 163–171. https://doi.org/10.1016/j.colsurfa.2010.01.043.

Mays, D.C., Hunt, J.R., 2005. Hydrodynamic aspects of particle clogging in porous media. Environ. Sci. Technol. 39 (2), 577–584. https://doi.org/10.1021/es049367k.

McDowell-Boyer, L.M., Hunt, J.R., Sitar, N., 1986. Particle transport through porous media. Water Resour. Res. 22 (13), 1901–1921. https://doi.org/10.1029/wr022i013p01901.

Moghadasi, J., Müller-Steinhagen, H., Jamialahmadi, M., Sharif, A., 2004. Theoretical and experimental study of particle movement and deposition in porous media during water injection. J. Petrol. Sci. Eng. 43 (3), 163–181. https://doi.org/10.1016/j.petrol.2004.01.005.

Purchas, D., Sutherland, K. (Eds.), 2002. Handbook of Filter Media. Elsevier. https://doi.org/10.1016/b978-185617375-9/50012-2.

Shevchenko, N., Boden, S., Eckert, S., Borin, D., Heinze, M., Odenbach, S., 2013. Application of X-ray radioscopic methods for characterization of two-phase phenomena and solidification processes in metallic melts. Eur. Phys. J. Special Top. 220 (1), 63–77. https://doi.org/10.1140/epjst/e2013-01797-y.

Sigloch, H., 2009. Technische Fluidmechanik. Springer, Berlin Heidelberg New York. https://doi.org/10.1007/978-3-642-03090-1.

Verwey, E.J.W., Overbeek, J.T.G., 1948. Theory of lyophobic colloids.

Waske, A., Heiland, M., Odenbach, S., 2012. Local position of colloid clusters in a packed bed of spheres. Chem. Eng. Sci. 76, 192–198. https://doi.org/10.1016/j.ces.2012.04.034.

Xu, S., Gao, B., Saiers, J.E., 2006. Straining of colloidal particles in saturated porous media. Water Resour. Res. 42 (12). https://doi.org/10.1029/2006wr004948.

Yao, K.M., Habibian, M.T., O'Melia, C.R., 1971. Water and waste water filtration. Concepts and applications. Environ. Sci. Technol. 5 (11), 1105–1112. https://doi.org/10.1016/s0015-1882(96)91323-3.

Yoon, J.S., Germaine, J.T., Culligan, P.J., 2006. Visualization of particle behavior within a porous medium: Mechanisms for particle filtration and retardation during downward transport. Water Resour. Res. 42 (6). https://doi.org/10.1029/2004wr003660.